

A Study of 2D Non-Stationary Massive MIMO Channels by Transformation of Delay and Angular Power Spectral Densities

Carlos F. López  and Cheng-Xiang Wang , *Fellow, IEEE*

Abstract—In this article, we propose a transformation method to model space-time-variant (STV) two-dimensional non-stationary wideband massive multiple-input multiple-output (MIMO) channels. This method enables us to obtain the STV joint probability density function of the time of arrival and angle of arrival (AOA) at any time instant and antenna element of the array from a predefined configuration of the scatterers. In addition, we introduce a simplified channel modeling approach based on STV parameters of the AOA distribution and demonstrate that key statistical properties of massive MIMO channels, such as the STV temporal autocorrelation function and Doppler power spectral density, can be derived in closed form. As examples of application, we study multiple array-variant properties of three widely-used geometry-based stochastic models (GBSMs): the Unified Disk, Ellipse, and Gaussian scattering models. Furthermore, we present numerical and simulation results of the statistical properties of these three GBSMs and compare them with those obtained using the conventional spherical wavefront approach. We point out possible limitations of the studied channel models to properly represent massive MIMO channels.

Index Terms—Array-variant angular and delay distributions, massive MIMO, non-stationary channel models, statistical properties, transformation method.

I. INTRODUCTION

IN RECENT years, multiple-input multiple-output (MIMO) technologies have enabled a remarkable increase in reliability, efficiency, and throughput of wireless communication

Manuscript received January 25, 2020; revised August 23, 2020; accepted October 15, 2020. Date of publication November 10, 2020; date of current version January 22, 2021. This work was supported in part by the National Key R&D Program of China under Grant 2018YFB1801101, in part by the National Natural Science Foundation of China under Grant 61960206006, in part by the Frontiers Science Center for Mobile Information Communication and Security, the High Level Innovation and Entrepreneurial Research Team Program in Jiangsu, the High Level Innovation and Entrepreneurial Talent Introduction Program in Jiangsu, the Research Fund of National Mobile Communications Research Laboratory, Southeast University, under Grant 2020B01, in part by the Fundamental Research Funds for the Central Universities under Grant 2242020R30001, in part by the EU H2020 5G Wireless project under Grant 641985, and in part by the EU H2020 RISE TESTBED2 project under Grant 872172. The review of this article was coordinated by Dr. Huiling Zhu. (Corresponding author: Cheng-Xiang Wang.)

Carlos F. López is with MathWorks, G2 2NR Glasgow, U.K. (e-mail: clopez@mathworks.com).

Cheng-Xiang Wang is with the National Mobile Communications Research Laboratory, School of Information Science and Engineering, Southeast University, Nanjing 210096, China, and Purple Mountain Laboratories, Nanjing 211111, China, and also with the Institute of Sensors, Signals and Systems, School of Engineering and Physical Sciences, Heriot-Watt University, EH14 4AS Edinburgh, U.K. (e-mail: chxwang@seu.edu.cn).

Digital Object Identifier 10.1109/TVT.2020.3037199

systems by employing multiple antennas on one or both sides of the communication link. Consequently, MIMO technologies have widely been adopted in modern wireless communication standards. In particular, massive MIMO, i.e., MIMO technologies incorporating a large number of antennas, has been proposed as a solution to cope with the exigent requirements of the fifth-generation (5G) wireless communication systems [1]–[3]. Despite the great challenges caused by employing a large number of antennas, massive MIMO can provide substantial gains as practical implementations have recently demonstrated [4]–[6]. However, important benefits of massive MIMO technologies, e.g., increased array gain, angular resolution, and diversity order, are intrinsically related to a sufficient separation between adjacent antennas and the total size of the antenna array [7]. Thus, as packing many antennas in very compact shapes is not always possible or desirable, massive MIMO deployments often result in antenna arrays spanning long distances, i.e., longer than the distance where the channel can be considered wide-sense stationary (WSS).

In order to assess and design new wireless communication technologies, it is of paramount importance to study and model the underlying propagation channels. Large-scale antenna arrays are subject to complex propagation effects, e.g., near-field region effects, not present in conventional MIMO communication systems. These effects have been demonstrated by measurements and they include array-varying angle of arrival (AOA), time of arrival (TOA), received power, and multipath components (MPCs) (dis)appearance among others [8]–[16]. Consequently, massive MIMO channels can often not be regarded as wide-sense stationary over the array [17].

In the past, time-domain non-WSS wireless channels were firstly studied to enable high-mobility communication systems [18], [19], e.g., vehicular and high-speed train [20], [21], due to their rapidly-varying characteristics. Recent high-mobility channel models [22], [23] employed the so called *parameters drifting*, i.e., time-variant channel parameters such as TOAs and AOAs, with increased theoretical and computational complexity. Conversely, the family of COST channel models, e.g., COST 207 [24] and COST 2100 [25], are intrinsically non-stationary in the time domain, but they determine the location of the clusters of scatterers in the environment from the specified angular and delay parameters and compute the exact distance between the scatterers and transceivers. A similar approach was used in recent works on massive MIMO channel modeling that

incorporated spherical [26]–[29] or parabolic wavefronts [30], [31]. Spherical and parabolic wavefronts compute the exact and second-order approximations to the distances between the scatterers and the antenna elements of the array, respectively. Similarly to the parameters-drifting approach, high-order wavefronts capture channel non-WSS properties over the array at the expense of high theoretical and computational complexity. However, channel models that can lead to closed-form expressions of their statistical properties can help develop new techniques that improve system performance [32].

In [26], [28], [29], the authors proposed two-dimensional (2D) [26] and three-dimensional (3D) [28], [29] wideband massive MIMO geometry-based stochastic models (GBSMs) that used spherical wavefronts, temporal parameter drifting, and space-time birth-death processes to capture near-field region effects and (dis)appearance of clustered MPCs, respectively. In [31], a 3D wideband massive MIMO GBSM was proposed, including parabolic wavefronts of reduced complexity, cluster (re)appearance and shadowing processes in time and space domains. Whereas the authors in [26], [28], [31] neglected variations of the TOA over the array, [29] considered them. However, none of these works studied the space-time-variant (STV) distribution of TOA and AOA.

The quasi-deterministic channel models QuaDRiGa [33] and mmMAGIC [34] employed a combined approach including spherical wavefronts and temporal parameters drifting. The stochastic COST 2100 [25], METIS [35], 3GPP-NR [36] and IMT-2020 [37] channel models did not consider spherical wavefronts and supported mobility at the mobile-station side only. Although COST 2100 [25] channel model did not originally support large-scale arrays, an extension was developed in [38] to incorporate spherical wavefronts and visibility regions over the array. The map-based deterministic METIS model and the quasi-deterministic MiWEBA [39] channel model implicitly included spherical wavefronts and temporal channel evolution through ray-tracing techniques with high computational complexity. Among these works, delay drifts over the array were only considered in QuaDRiGa [33], map-based METIS [35], and the extended COST 2100 [38] models. However, these works [33], [35], [38] did not study the effects of delay drifts on the statistical properties of massive MIMO channels and none of the works above studied the STV distribution of TOA and AOA.

In [40], the authors employed the theory of transformation of random variables to investigate the spatial configuration of the scatterers in multiple coordinate systems for predefined joint probability density functions (PDFs) of the AOA and TOA. Similar investigations were conducted in the past for specific GBSMs [41], [42], but they did not study non-WSS channels in space or time domains.

In previous works [43], we reported preliminary results on the delay drift over the array. However, we only studied the Ellipse channel model and focused on the TOA variations over the array, neglecting the spatial-temporal variations of the joint PDF of the TOA and AOA. Theoretical studies on the STV joint PDF of the TOA and AOA and space-time parameters drifting for non-WSS massive MIMO channels are still missing. Moreover, the equivalence of the spherical wavefront and

parameters drifting approaches to model the statistical properties of massive MIMO channels has not been investigated yet. To fill these gaps, we propose a transformation method to theoretically study spatial-temporal non-stationary wideband massive MIMO channels. The proposed method employs the theory of transformation of random variables and geometrical mappings in multiple coordinate systems to model the STV joint PDF of the TOA and AOA for the first time. It also enables us to obtain analytical expressions of the STV scattering function (SF), delay and angular power spectral densities (PSDs) for arbitrary configurations of the scatterers. In addition, we propose an approximation method to obtain the STV angular spread, which was not considered in previous theoretical studies of massive MIMO channels. Next, we highlight the **contributions and novelties** of this article:

- 1) We propose a general transformation method to model the STV joint PDF of the TOA and AOA for 2D non-WSS massive MIMO channels. For the first time, we derive closed-form expressions of this joint-PDF for the three most common ways of specifying the distribution of the scatterers, e.g., in the TOA-AOA, polar, and Cartesian domains, and for arbitrary-shaped 2D arrays. Through numerical evaluation and simulation, we demonstrate the equivalence of the proposed methods and the spherical-wavefront approach to capture the statistical properties of the channel.
- 2) We obtain approximate expressions for the STV angular spread of the channel when the AOA follows a von Mises distribution. Additionally, we employ the STV angular spread to approximate new closed-form solutions of key statistical properties of massive MIMO channels, such as the temporal autocorrelation function (ACF) and the Doppler PSD.
- 3) We study the STV joint PDFs of the AOA and TOA of widely-used MIMO GBSMs such as the Ellipse, Unified Disk, and Gaussian scattering models. In all cases, we show that the joint PDFs of the AOA and TOA are subject to drifting and spreading over the array. Besides, we study the frequency correlation function (FCF) of these GBSMs and show that its array-varying properties are caused not only by the disappearance of MPCs, but also by the drift and spread of the TOA over the array.
- 4) We describe some limitations of existing MIMO GBSMs that were upgraded to simulate massive MIMO channels, e.g., the Unified Disk, Ellipse, and Gaussian scattering models, due to the array-variant characteristics of the joint PDF of the TOA and AOA.

The rest of this article is organized as follows. In Section II, we present the non-stationary wideband massive MIMO channel model employed in the following sections. In Section III, we derive the general transformation method for the three most-used coordinate systems. Section IV applies the transformation method to widely-used MIMO channel models such as the Ellipse or Gaussian cluster models. The derivation of key statistical properties of the channel from the transformed joint PDF of the TOA and AOA is presented in Section V. In Section VI, we show the good agreement between the statistical properties obtained

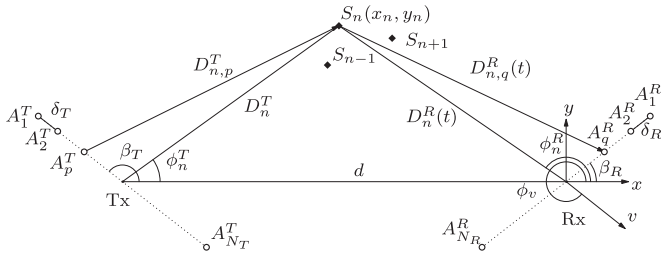


Fig. 1. A 2D wideband massive MIMO channel model.

through the proposed methods and the spherical wavefront approach. Conclusions are drawn in Section VII.

II. A 2D WIDEBAND MASSIVE MIMO STOCHASTIC CHANNEL MODEL

Let us consider a 2D wideband massive MIMO channel model depicted in Fig. 1 where the transmitter (Tx) and receiver (Rx) are equipped with uniform linear antenna arrays (ULAs). The transmitting (receiving) ULA is composed of N_T (N_R) omnidirectional antenna elements equally spaced with a distance δ_T (δ_R) and it is tilted at an angle β_T (β_R) with respect to (w.r.t.) the x -axis of a Cartesian coordinate system centered at the receiving array's center. The p -th ($p = 1, 2, \dots, N_T$) transmitting and q -th ($q = 1, 2, \dots, N_R$) receiving antenna elements are denoted by A_p^T and A_q^R , respectively. We assume that the signal is omnidirectionally bounced only once by each scatterer, denoted by S_n ($n = 1, 2, \dots, N_S$), and it travels a distance $D_{n,qp}(t) = D_{n,p}^T + D_{n,q}^R(t)$ from A_p^T to A_q^R via S_n at time instant t . Normally, the phase shifts θ_n introduced by the scatterers are modeled as independent and identically distributed (i.i.d.) random variables obeying a uniform distribution over $[0, 2\pi)$ [44]. The massive MIMO channel is represented by the matrix $\mathbf{H}(t, \tau) = [h_{qp}(t, \tau)]_{N_R \times N_T}$ whose entries denote the channel impulse response (CIR) between the antennas A_p^T and A_q^R . The CIR is given by

$$h_{qp}(t, \tau) = \sum_{n=1}^{N_S} c_n e^{j\psi_{n,qp}(t)} \delta(\tau - \tau_{n,qp}(t)) \quad (1)$$

where $j = \sqrt{-1}$, $\delta(\cdot)$ is the Dirac delta function. The term $\psi_{n,qp}(t) = k_0 D_{n,qp}(t) + \theta_n$ denotes the phase of the signal, $k_0 = 2\pi/\lambda$, and λ denotes the carrier wavelength. The n -th scattered signal is received with amplitude c_n and its associated propagation delay is $\tau_{n,qp}(t) = D_{n,qp}(t)/c_0$, where c_0 denotes the speed of light. Since signals from and to sufficiently separated antenna elements of the array experience different TOAs, $\tau_{n,qp}(t)$ in (1) depends on the antenna indices p and q . The channel transfer function (CTF), i.e., the Fourier transform of the CIR w.r.t. τ , is given by

$$H_{qp}(t, f) = \sum_{n=1}^{N_S} c_n e^{j\psi_{n,qp}(t)} e^{-j2\pi f \tau_{n,qp}(t)}. \quad (2)$$

For simplicity, we assume that the center of the receiving array is located at the origin at $t = 0$ and it moves at a constant speed v forming an angle ϕ_v w.r.t. the x -axis. The Tx is static and

located at a distance d from the Rx along the negative x -axis. Accordingly, the distance traveled by the signal radiated by A_p^T and received by A_q^R via S_n can be computed as

$$D_{n,qp}(t) = \sqrt{(x_n - x_q^R - v_x t)^2 + (y_n - y_q^R - v_y t)^2} + \sqrt{(x_n + d - x_p^T)^2 + (y_n - y_p^T)^2} \quad (3)$$

where (x_n, y_n) denote the Cartesian coordinates of S_n . The terms $x_q^R = \delta_q^R \cos(\beta_R)$ and $y_q^R = \delta_q^R \sin(\beta_R)$ with $\delta_q^R = (N_R - 2q + 1)\delta_R/2$ denote the Cartesian coordinates of the antenna A_q^R at $t = 0$. Similarly, $x_p^T = \delta_p^T \cos(\beta_T)$ and $y_p^T = \delta_p^T \sin(\beta_T)$ with $\delta_p^T = (N_T - 2p + 1)\delta_T/2$ are the projections of the position vector of A_p^T w.r.t. the center of the transmitting array onto x and y axes, respectively. The Cartesian components of the velocity vector are $v_x = v \cos(\phi_v)$ and $v_y = v \sin(\phi_v)$.

A. Spherical and Plane Wavefronts

Spherical wavefronts are considered in the model as long as (3) is used to compute the phase of the signal $\psi_{n,qp}(t)$ in (1). The conventional approximation for short periods of time and small arrays, i.e., the first-order or plane wavefront approximation, reduces the distance $D_{n,qp}(t)$ to

$$D_{n,qp}(t) \approx D_n - \delta_p^T \cos(\phi_n^T - \beta_T) - \delta_q^R \cos(\phi_n^R - \beta_R) - vt \cos(\phi_n^R - \phi_v) \quad (4)$$

where $D_n = D_n^T + D_n^R(0) = \sqrt{(x_n + d)^2 + y_n^2} + \sqrt{x_n^2 + y_n^2}$ denotes the distance between the arrays' centers, and the terms ϕ_n^T and ϕ_n^R denote the angle of departure (AOD) and AOA of the n -th scattered signal w.r.t. to the arrays' centers, which can be calculated as $\phi_n^R = \arctan(y_n/x_n)$ and $\phi_n^T = \arctan(y_n/(x_n + d))$. Equation (4) can be obtained by replacing $\delta_p^T = \hat{x} D_n^T$, $\delta_q^R = \hat{y} D_n^R(0)$, $vt = \hat{z} D_n^R(0)$ in (3) and using a first-order Taylor approximation of the two radicals with respect to \hat{x} , \hat{y} , and \hat{z} .

In spatial WSS non-massive MIMO channel models, the plane-wavefront approximation in (4) is usually employed to compute the phase of the signal in (1) [44]. From (1) and (4), it can be seen that this approximation leads to linear space-time variations of the phase, which do not allow to capture the non-WSS properties of massive MIMO channels. In addition, the TOA $\tau_{n,qp}(t)$ in (1) and (2) is usually approximated as a constant value for every scatterer, i.e., $\tau_{n,qp}(t) = \tau_n$. This assumption may be inaccurate for large antenna arrays.

III. A TRANSFORMATION METHOD OF THE STV JOINT PDF OF THE TOA AND AOA

In conventional WSS GBSMs [44], scatterers are assumed to be randomly distributed in the environment according to a predefined PDF that models the TOA and AOA of the received signal, and this PDF is space-time-frequency independent [40]. Unlike WSS channels, measurements [8]–[16] have shown that TOAs and AOAs may change over the array and time for large arrays and periods of time, respectively. In this section, we introduce a method based on the transformation of random

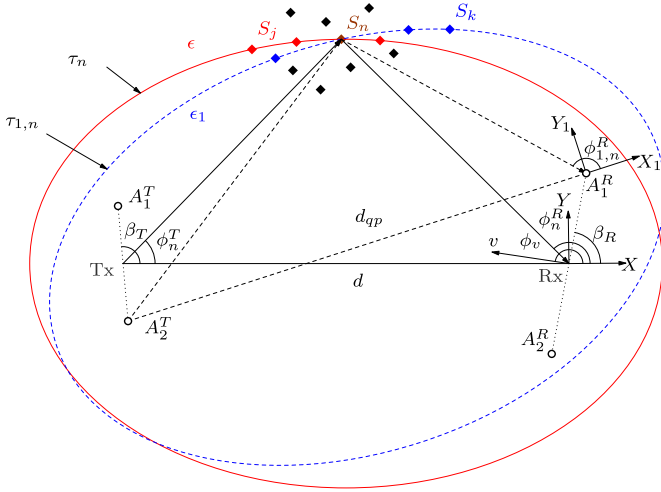


Fig. 2. Elements of the transformation of the joint PDF of the TOA and AOA at $t = 0$.

variables to obtain the STV joint PDF of TOA-AOA for every antenna pair $A_p^T - A_q^R$ at any time instant t . The method proposed is developed for the three most common domains used to specify the distribution of the scatterers: TOA-AOA, Polar, and Cartesian domains.

A. Transformation in TOA-AOA Domain

For clarity, the most important elements of the TOA-AOA transformation are illustrated geometrically in Fig. 2 for a MIMO system employing 2×2 antennas at time instant $t = 0$. Note that we have depicted ULAs for convenience, but the proposed method is not limited to any arrangement of the antenna arrays, i.e., it can be applied to arbitrary-shaped 2D arrays. The origins of the Cartesian coordinate systems (X, Y) and (X_1, Y_1) are located at the center of the receiving array and A_1^R , respectively. The AOA of the signal scattered by S_n and measured at (X, Y) and (X_1, Y_1) are denoted by ϕ_n^R and $\phi_{1,n}^R$, respectively. Signals radiated from the center of the transmitting array and bounced by the scatterers located in the ellipse ϵ , e.g., S_j and S_n , arrive at the center of the receiving array with the same TOA, which is denoted as τ_n . Likewise, the ellipse ϵ_1 illustrates the same concept as ϵ when the signals transmitted from A_2^T and received at A_1^R experience a constant delay denoted as $\tau_{1,n}$.

The direct transformation of the random TOA and AOA measured at the center of the array (τ, ϕ^R) to the TOA and AOA measured at any antenna element and time instant t (τ_1, ϕ_1^R) is defined as

$$\tau = c_0^{-1} \left(\sqrt{x^2 + y^2} + \sqrt{(x+d)^2 + y^2} \right) \quad (5)$$

$$\phi^R = \arctan(y/x) \quad (6)$$

with

$$x = \frac{1}{2} \left[\frac{(c_0\tau_1)^2 - d_{qp}^2(t)}{c_0\tau_1 + d_{qp}(t) \cos \phi_1^R} \right] \cos(\phi_1^R + \alpha_{qp}(t)) + x_q^R + v_x t \quad (7)$$

$$y = \frac{1}{2} \left[\frac{(c_0\tau_1)^2 - d_{qp}^2(t)}{c_0\tau_1 + d_{qp}(t) \cos \phi_1^R} \right] \sin(\phi_1^R + \alpha_{qp}(t)) + y_q^R + v_y t. \quad (8)$$

The parameter $d_{qp}(t)$ denotes the distance between A_p^T and A_q^R and $\alpha_{qp}(t)$ the angle between the segment joining A_p^T and A_q^R and the x -axis at time instant t . These parameters are calculated in Appendix A.

As the direct transformation of the random TOA and AOA is rather complicated and leads to cumbersome expressions for the Jacobian determinant, we use a stepped approach to obtain the STV joint PDF of TOA-AOA. The distribution of the TOA-AOA of a signal radiated from A_2^T and received at A_1^R can be obtained using the following steps:

- 1) From a given distribution of TOA-AOA $f_{\tau, \phi^R}(\tau, \phi^R)$, the joint PDF of the location of the scatterers $f_{XY}(x, y)$ in the Cartesian coordinates (X, Y) is derived as proposed in [40]. The transformation of the random variables (τ, ϕ^R) is indeed a transformation of coordinates.
- 2) A second transformation is performed from (X, Y) into (X_1, Y_1) , resulting in the PDF $f_{X_1 Y_1}(x_1, y_1)$. These two coordinate systems are related by shift and rotation operations according to the relative positions of the antennas A_2^T and A_1^R .
- 3) The locations of the scatterers in the system (X_1, Y_1) are transformed back into the TOA-AOA domain, obtaining the PDF $f_{\tau_1, \phi_1^R}(\tau_1, \phi_1^R)$ for the antenna elements A_2^T and A_1^R .

Using the previous approach, the joint PDF can be obtained as (see Appendix A)

$$f_{\tau_1, \phi_1^R}(\tau_1, \phi_1^R) = (|J_1(x, y)| |J_3(\tau_1, \phi_1^R)|)^{-1} f_{\tau, \phi^R}(\tau, \phi^R) \quad (9)$$

where τ and ϕ^R were obtained in (5)–(8), respectively. The Jacobian determinants $J_1(x, y)$ and $J_3(\tau_1, \phi_1^R)$ can be found in Appendix A. Notice that the actual AOA measured from A_q^R is not ϕ_1^R but $\phi_1^R - \alpha_{qp}(t)$ due to the rotation of the coordinate system (X_1, Y_1) w.r.t. (X, Y) . It can be seen that for small arrays and periods of time, i.e., $\delta_{M_T}^T \ll (c_0\tau - d)$, $\delta_{M_R}^R \ll (c_0\tau - d)$, and $vt \ll (c_0\tau - d)$, then $|J_1(x, y)|^{-1} |J_3(\tau_1, \phi_1^R)|^{-1} \approx 1$, $\alpha_{qp}(t) \approx 0$, $d_{qp}(t) \approx d$, and $f_{\tau_1, \phi_1^R}(\tau_1, \phi_1^R) \approx f_{\tau, \phi^R}(\tau, \phi^R)$. Thus, when the joint PDF of TOA-AOA is independent of the antenna element and time instant, the channel can be considered as WSS.

The main advantage of this stepped approach compared to the direct one from (τ, ϕ^R) to (τ_1, ϕ_1^R) is that the equations of the Jacobian determinants J_1 and J_3 can be reused for other specifications of the scatterers' distribution in different domains such as (14) and (15). In addition, the expressions for the Jacobian determinants of the transformations are simpler.

It is important to highlight the difference between the transformation method proposed and the ones used in previous theoretical works (e.g., [45]–[47] and [26]–[28]). In the proposed method, the parameters that define $f_{\tau, \phi^R}(\tau, \phi^R)$ are space-time invariant, but this distribution gets transformed for different antenna elements of the arrays and time instants. In those previous

works, it was assumed that only some parameters, e.g., the mean AOA, defining the distribution are STV, but the distribution remained space-time invariant. The previous approach is an approximation that may only hold in some limited cases as we will show in subsequent sections.

B. Transformation in Polar Domain

Analogous to the previous section, the PDF of the position of the scatterers is transformed in three steps. However, as the given PDF is defined in polar coordinates, i.e., $f_{R,\phi^R}(r, \phi^R)$, the first transformation of the random variables (r, ϕ^R) to (X, Y) is performed using $X = R \cos(\phi^R)$ and $Y = R \sin(\phi^R)$. The joint PDF of (X, Y) is given by

$$f_{X,Y}(x, y) = |J_1(x, y)|^{-1} f_{R,\phi^R}(r, \phi^R) \quad (10)$$

where

$$r = \sqrt{x^2 + y^2} \quad (11)$$

$$\phi^R = \arctan(y/x) \quad (12)$$

and $J_1(x, y)$ is the Jacobian of the transformation, i.e.,

$$|J_1(x, y)|^{-1} = \left| \frac{1}{\sqrt{x^2 + y^2}} \right|. \quad (13)$$

Finally, the joint PDF of (τ_1, ϕ_1^R) can be obtained as

$$f_{\tau_1, \phi_1^R}(\tau_1, \phi_1^R) = (|J_1(x, y)| |J_3(\tau_1, \phi_1^R)|)^{-1} f_{R,\phi^R}(r, \phi^R) \quad (14)$$

where $|J_3(\tau_1, \phi_1^R)|^{-1}$, x , and y are defined in (45), (7), and (8), respectively.

C. Transformation in Cartesian Domain

In this case, the transformation procedure is reduced to two steps as it is not necessary to perform a transformation to Cartesian coordinates. Thus, the joint PDF $f_{\tau_1, \phi_1^R}(\tau_1, \phi_1^R)$ is a function of the joint PDF $f_{X,Y}(x, y)$ and is obtained as

$$f_{\tau_1, \phi_1^R}(\tau_1, \phi_1^R) = |J_3(\tau_1, \phi_1^R)|^{-1} f_{X,Y}(x, y) \quad (15)$$

where x and y are defined in (7) and (8), respectively.

IV. APPLICATION OF THE TRANSFORMATION METHOD TO MIMO CHANNEL MODELS

In this section, the transformation method described in Section III is applied to study the TOA-AOA variations across the array of widely-used channel models defined in each of the three different domains. For the TOA-AOA domain, the Ellipse narrowband and wideband channel models are studied. For the Polar domain, the one-ring model and unified disk scattering model (UDSM) are analyzed. For the Cartesian domain, the Gaussian cluster channel model is employed.

1) *Ellipse Narrowband and Wideband Channel Models*: In the Ellipse channel model, the scatterers are located in the perimeter of an ellipse with foci at the center of the transmitting and receiving arrays. In the single-ellipse model, the TOA is

fixed to a single value τ_0 , but the AOA distribution is not defined. In this article, we will employ the von Mises distribution to model the AOA as an example, as it can cover both isotropic and non-isotropic angular distributions through its parameters [44], [48]. For large values of its concentration parameter κ , the von Mises distribution accurately approximates a Gaussian distribution, which has been widely reported and used in standard-based channel models such as 3GPP-NR [36]. The joint PDF is given by

$$f_{\tau, \phi^R}(\tau, \phi^R) = \delta(\tau - \tau_0) \cdot \frac{1}{2\pi I_0(\kappa)} e^{\kappa \cos(\phi^R - \mu^\phi)} \quad (16)$$

where μ^ϕ and κ are the mean AOA and concentration parameter, respectively, and $I_0(\cdot)$ denotes the zero-order modified Bessel function of the first kind. It is important to remark that (16) implies independent time dispersion and frequency dispersion [44], i.e., its joint PDF of TOA-AOA is separable, and is also a narrowband channel model, i.e., the absolute value of the FCF is constant. A more flexible distribution that includes the previous one as a special case and permits to capture wideband characteristics of the channel is

$$f_{\tau, \phi^R}(\tau, \phi^R) = \frac{e^{-\frac{(\tau - \tau_0)}{\sigma_\tau}}}{\sigma_\tau} u(\tau - \tau_0) \frac{1}{2\pi I_0(\kappa)} e^{\kappa \cos(\phi^R - \mu^\phi)} \quad (17)$$

where $u(\cdot)$ denotes the unit-step function, i.e., $u(x) = 1$ for $x > 0$ and zero otherwise. Note that the marginal distribution of delays $\delta(\tau - \tau_0)$ in (16) has been substituted in (17) by a shifted exponential distribution with minimum delay τ_0 and standard deviation σ_τ , which denotes the delay spread of the channel. The unit-step function is used to guarantee that the model is causal. It is clear that as $\sigma_\tau \rightarrow 0$, the PDF in (17) converges to that in (16). From the communications system's perspective, as long as σ_τ is much smaller than the time-resolution of the system considered, both distributions model equivalent channels. The transformed PDFs at the antennas A_p^T , A_q^R and time instant t can be obtained by plugging (16) and (17) into (9). As it will be shown in the results presented in Section VI, the transformation of (16) breaks down the separability of the distribution of TOA-AOA, introducing a dependence between these two random variables. This can be easily seen by noting that the term $\delta(\tau - \tau_0)$ in (16) is transformed into $\delta(c_0^{-1}[\sqrt{x^2 + y^2} + \sqrt{(x+d)^2 + y^2}] - \tau_0)$, with x and y given by (7) and (8), respectively. As the values of ϕ_1^R that solve $\sqrt{x^2 + y^2} + \sqrt{(x+d)^2 + y^2} = c_0\tau_0$ depend on the the delay τ_1 , the TOA and AOA are dependent and therefore correlated. As this argument can be applied to any separable distribution, the important *independent time dispersive and Doppler frequency dispersive* property [44] of the Ellipse and other channel models is broken down by the large dimensions of the array.

2) *One-Ring Model and Unified Disk Scattering Model (UDSM)*: The One-Ring model defines the geometrical configuration of the scatterers in a circular ring around the center of the receiving array. This geometry is usually applied to model narrowband channels, although its delay spread is not zero and varies according to the radius of the ring and the distribution of

the AOA [49]. Using the von Mises distribution for the AOA, the PDF of the position of the scatterers in polar coordinates is given by

$$f_{R,\phi^R}(r, \phi^R) = \delta(r - r_0) \cdot \frac{1}{2\pi I_0(\kappa)} e^{\kappa \cos(\phi^R - \mu^\phi)} \quad (18)$$

where r_0 is the radius of the ring. A more flexible distribution that includes the one-ring model as a special case is the UDSM [50]. Although the UDSM is constrained to uniform distributions of the AOA, the PDF of the position of the scatterers can be extended to account for non-uniform distributions as

$$f_{r,\phi^R}(r, \phi^R) = \frac{(k_U + 1)}{r_0^{(k_U+1)}} r^{k_U} \cdot [u(r) - u(r - r_0)] \times \frac{1}{2\pi I_0(\kappa)} e^{\kappa \cos(\phi^R - \mu^\phi)} \quad (19)$$

where $k_U > -1$ is a real-valued parameter called the shape factor that controls the spread of the scatterers w.r.t. the radial distance. As $k_U \rightarrow \infty$, the scatterers become more concentrated near the edge of the disk forming a ring of radius r_0 and (19) converges to (18). The transformed PDFs at the antennas A_p^T , A_q^R and time instant t can be obtained by plugging (18) and (19) into (14). The resulting PDFs are omitted here for brevity.

3) *Gaussian Cluster Channel Model*: The Gaussian cluster model has widely been used in multiple standard GBSMs, e.g., COST 207 [24] and COST 2100 [25], to model single- and multi-bounce clustered MPCs including intracluster delay and angle spreads. A simplified PDF of the position of the scatterers for this model in Cartesian coordinates is given by

$$f_{X,Y}(x, y) = \frac{1}{2\pi\sigma_{xy}^2} e^{-\frac{1}{2\sigma_{xy}^2} [(x-x_0)^2 + (y-y_0)^2]} \quad (20)$$

where (x_0, y_0) denote the coordinates of the center of the cluster and σ_{xy} the spread of the cluster in the xy -plane. Note that the spreads of the cluster in the x and y axes are assumed to be equal here for simplicity. The joint PDF $f_{\tau_1, \phi_1^R}(\tau_1, \phi_1^R)$ can be obtained by plugging (20) into (15). The resulting PDF is omitted here for brevity.

V. STATISTICAL PROPERTIES OF MASSIVE MIMO CHANNELS

In the following, the STV PDF $f_{\tau_1, \phi_1^R}(\tau_1, \phi_1^R)$ obtained in Section III will be used to compute the STV statistical properties of the channel such as the Doppler, delay, and angular PSDs, and the space-time-frequency cross-correlation function (STF-CCF).

A. Computation of Statistical Properties From the Transformed Distribution of the TOA-AOA

1) *Delay PSD*: The delay PSD or power delay profile (PDP) is a measure of the distribution of the received power in the delay domain. It can be seen that the PDP is proportional to the distribution of the TOA of the received signal [44, p. 348]. Accordingly, the STV PDP can be obtained through the marginal PDF of τ_1 as $S_{\tau_1}(\tau_1) = \sigma_0^2 f_{\tau_1}(\tau_1)$ where σ_0^2 denotes the total received power and $f_{\tau_1}(\tau_1)$ denotes the marginal PDF of the TOA.

2) *Angular PSD*: Similarly, the angular PSD or power angular spectrum (PAS) is a measure of the incoming power in the angular domain. Thus, the STV PAS can be analogously obtained through the marginal PDF of the AOA ϕ_1^R as $S_{\phi_1^R}(\phi_1^R) = \sigma_0^2 f_{\phi_1^R}(\phi_1^R)$ where $f_{\phi_1^R}(\phi_1^R)$ denotes the marginal PDF of the AOA.

3) *Doppler PSD*: For a mobile station moving at a constant speed v and direction defined by the angle ϕ_v , and a set of static scatterers, the Doppler frequency ν is a function of the AOA as $\nu = \nu_{\max} \cos(\phi_1^R - \phi_v)$, where $\nu_{\max} = v/\lambda$ denotes the maximum Doppler frequency. According to this definition, it can be proved that the Doppler PSD is given by [44]

$$S_\nu(\nu) = \frac{2\sigma_0}{\nu_{\max} \sqrt{1 - (\nu/\nu_{\max})^2}} g_{\phi_1^R}(\arccos[\nu/\nu_{\max}]) \quad (21)$$

where

$$g_{\phi_1^R}(\phi_1^R) = \frac{1}{2} (f_{\phi_1^R}(\phi_1^R) + f_{\phi_1^R}(-\phi_1^R)) \quad (22)$$

is the even part of the STV PDF of the AOA.

4) *Space-Time-Frequency Cross-Correlation Function (STF-CCF)*: In the proposed approach, the cross-correlation between the signal corresponding to the link $A_p^T - A_q^R$ at time instant t and frequency f , and that of the link $A_{p'}^T - A_{q'}^R$ at time $t + \Delta t$ and frequency $f + \Delta f$ can be obtained as $\rho_{qp, q'p'}(t, \Delta t, \Delta f) = \mathbb{E}[H_{qp}(t, f) H_{q'p'}^*(t + \Delta t, f + \Delta f)]$, with $\mathbb{E}(\cdot)$ denoting the expectation operator and H^* the complex conjugate of H . Thus, the STF-CCF can be computed as

$$\rho_{qp, q'p'}(t, \Delta t, \Delta f) = \sigma_0^2 \int_0^\infty \int_0^{2\pi} e^{-jk_0 \Psi_{qp}^{q'p'}(t, \Delta t)} e^{-j2\pi \Delta f \tau_1} \times f_{\tau_1, \phi_1^R}(\tau_1, \phi_1^R) d\tau_1 d\phi_1^R \quad (23)$$

where $\Psi_{qp}^{q'p'}(t, \Delta t) = \Delta_{pp'} \cos(\phi_1^T - \beta_T + \alpha_{qp}(t)) + \Delta_{qq'} \cos(\phi_1^R - \beta_R + \alpha_{qp}(t)) + v\Delta t \cos(\phi_1^R - \phi_v + \alpha_{qp}(t))$ denotes the phase difference between the signal transmitted from A_p^T and received by A_q^R at time t and the signal transmitted from $A_{p'}^T$ and received by $A_{q'}^R$ at $t + \Delta t$. The distance between A_p^T and $A_{p'}^T$ is $\Delta_{pp'} = (p - p')\delta_T$, and that between A_q^R and $A_{q'}^R$ is $\Delta_{qq'} = (q - q')\delta_R$. It is worth noting that near-field region effects, which are usually modeled using spherical wavefronts, are captured in the proposed method by the space-time variant PDF of the TOA and AOA.

When the spherical wavefront is used, the STF-CCF can be calculated as [27]

$$\hat{\rho}_{qp, q'p'}(t, \Delta t, \Delta f) = \sigma_0^2 \int_0^\infty \int_0^{2\pi} e^{-jk_0 \hat{\Psi}_{qp}^{q'p'}(t, \Delta t)} e^{-j2\pi \Delta f \tau} \times f_{\tau, \phi^R}(\tau, \phi^R) d\tau d\phi^R \quad (24)$$

where $\hat{\Psi}_{qp}^{q'p'}(t, \Delta t) = D_{qp}(t) - D_{q'p'}(t + \Delta t)$ and $D_{qp}(t)$ denotes the total distance traveled by the signal from A_p^T to A_q^R at time instant t as given by (3). Notice that the TOA and AOA used in (24) are defined at the center of the transmitting and receiving arrays at time $t = 0$ and they are space-time invariant. Consequently, the spherical wavefront is required to capture

non-WSS properties of the channel and the plane wavefront approximation in (4) cannot be used.

With respect to the deterministic simulation model as defined in (1) and (2) once the random variables involved are drawn, the STF-CCF can be approximated as a local time-average, i.e.,

$$\tilde{\rho}_{qp,q'p'}(t, \Delta t, \Delta f) \approx \frac{1}{T} \int_{t_1}^{t_2} H_{qp}(t', f) \times H_{q'p'}^*(t' + \Delta t, f + \Delta f) dt' \quad (25)$$

where $t_1 = t - T/2$ and $t_2 = t + T/2$. The temporal ACFs can be obtained by setting $\Delta f = \Delta_{qq'} = \Delta_{pp'} = 0$ in (23), (24), and (25) as $\rho_{qp,qp}(t, \Delta t, 0)$, $\hat{\rho}_{qp,qp}(t, \Delta t, 0)$, and $\tilde{\rho}_{qp,qp}(t, \Delta t, 0)$, respectively. By setting $\Delta t = \Delta f = 0$ in the same equations, we can calculate the spatial cross-correlation functions (S-CCFs) as $\rho_{qp,q'p'}(t, 0, 0)$, $\hat{\rho}_{qp,q'p'}(t, 0, 0)$, and $\tilde{\rho}_{qp,q'p'}(t, 0, 0)$. The FCFs are computed by setting $\Delta_{qq'} = \Delta_{pp'} = \Delta t = 0$ as $\rho_{qp,qp}(t, 0, \Delta f)$, $\hat{\rho}_{qp,qp}(t, 0, \Delta f)$, and $\tilde{\rho}_{qp,qp}(t, 0, \Delta f)$. The ACFs, S-CCFs, and FCFs obtained depend on the antenna indices and the time instant through τ_1 and ϕ_1^R in (23) and through the total distance in $\hat{\Psi}_{qp}^{q'p'}(t, \Delta t)$ in (24), indicating that the channel is space-time non-WSS.

B. Approximate Solutions to the ACF and Doppler PSD

Although analytic solutions for the STF-CCF in (23) are difficult to obtain due to the complexity of the STV joint PDF of the TOA and AOA, approximate expressions for the ACF, Doppler PSD, and S-CCF can be derived for non-WSS massive MIMO channels. We propose a simplified approach based on an implicit assumption of previous works, e.g., [51] and [45], in which the PAS was assumed space-time invariant, but some of its parameters were not.

Let us consider that the AOA defined at the center of the array (ϕ^R) follows a von Mises distribution with parameters (κ, μ^ϕ) . Then, if we assume that only the parameters of this distribution are STV, the PDF of the AOA for any A_p^T, A_q^R and time instant t becomes

$$f_{\phi_1^R}(\phi_1^R) = \frac{1}{2\pi I_0(\kappa_{qp}(t))} e^{\kappa_{qp}(t) \cos(\phi_1^R - \mu_{qp}^\phi(t))} \quad (26)$$

where the mean AOA $\mu_{qp}^\phi(t)$ and concentration parameter $\kappa_{qp}(t)$ are now dependent of time and antenna indices. In slowly varying channels, we can assume that the rates of change of $\mu_{qp}^\phi(t)$ and $\kappa_{qp}(t)$ are small. Consequently, these parameters can be considered approximately constant for short intervals of the array and periods of time. If the spatial-temporal evolution of these parameters is known, the STV ACF can be approximated as [44]

$$\rho(\Delta t; \delta_p^T, \delta_q^R, t) \approx \frac{2\sigma_0^2}{I_0(\kappa_{qp}(t))} I_0 \left([\kappa_{qp}^2(t) - (2\pi\nu_{\max} \Delta t)^2 - j4\pi\kappa_{qp}(t)\nu_{\max}\Delta t \cos(\mu_{qp}^\phi(t) - \phi_v)]^{\frac{1}{2}} \right) \quad (27)$$

As the parameters $\mu_{qp}^\phi(t)$ and $\kappa_{qp}(t)$ depend on the position over the array and time instant, the channel is non-WSS in these domains. Similarly, according to (21), the STV Doppler PSD is

$$S_\nu(\nu) \approx \frac{2\sigma_0^2 e^{\kappa_{qp}^2(t) \cos(\mu_{qp}^\phi(t) - \phi_v)\nu/\nu_{\max}}}{\pi\nu_{\max} I_0(\kappa_{qp}^2(t)) \sqrt{1 - (\nu/\nu_{\max})^2}} \times \cosh \left(\kappa_{qp}^2(t) \sin(\mu_{qp}^\phi(t) - \phi_v) \sqrt{1 - (\nu/\nu_{\max})^2} \right) \quad (28)$$

In Appendix B, we derive approximate solutions of the STV concentration $\kappa_{qp}(t)$ and mean AOA $\mu_{qp}^\phi(t)$ as

$$\kappa_{qp}(t) = \kappa \left(1 + \left(\frac{\delta_q^R}{r_c} \right)^2 + \left(\frac{vt}{r_c} \right)^2 - 2 \frac{\delta_q^R}{r_c} \cos(\mu_c^\phi - \beta_R) - 2 \frac{vt}{r_c} \cos(\mu_c^\phi - \phi_v) + 2 \frac{vt\delta_q^R}{r_c^2} \cos(\beta_R - \phi_v) \right) \quad (29)$$

and

$$\mu_{qp}^\phi(t) = \arctan(\xi) \quad (30)$$

with

$$\xi = \frac{r_c \sin(\mu_c^\phi) - \delta_q^R \sin(\beta_R) - vt \sin(\phi_v)}{r_c \cos(\mu_c^\phi) - \delta_q^R \cos(\beta_R) - vt \cos(\phi_v)} \quad (31)$$

It can be easily seen that, for small arrays and short periods of time, i.e., $M_R \delta_R / 2 \ll r_c$ and $vt \ll r_c$, the concentration parameter and mean AOA become invariant, i.e., $\kappa_{c,q}(t) \approx \kappa_c$ and $\mu_{qp}^\phi(t) \approx \mu_c^\phi$.

VI. RESULTS AND ANALYSIS

In this section, we will present and compare the array-variant distribution of channel parameters and statistical properties obtained using the proposed transformation method, approximation method, spherical wavefront approach, and simulation results, for three channel models introduced in Section III. The results corresponding to the transformation method were obtained by numerical evaluation of (9), (14), and (15). Similarly, those corresponding to the approximation method were computed by evaluating (27)–(28) and making use of the variant parameters as determined by (29) and (30). We evaluated (24) to obtain the results corresponding to the spherical wavefront approach. For the simulation results, we generated 10^3 scatterers randomly distributed and computed the CIR as in (2). Realizations of the channel parameters, e.g., TOA and AOA, were obtained by the inverse transform sampling method [52]. To obtain the simulation results, the statistical properties were computed by averaging 10^3 realizations of the STF-CCF in (25).

In the following, we assume that no line-of-sight path exists between the Tx and Rx, which are located 100 m apart along the x -axis at $t = 0$ and both count on ULAs composed of 100 antenna elements each. The separation between adjacent antennas is $\lambda/2$ at 2 GHz of carrier frequency.

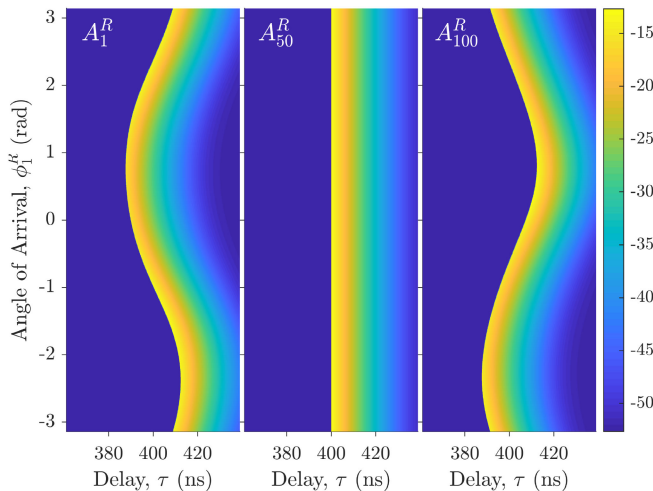


Fig. 3. Joint PDFs of the TOA and AOA at A_1^R (left), A_{50}^R (center), and A_{100}^R (right), for the wideband Ellipse channel model in (17) ($d = 100$ m, $f_c = 2$ GHz, $\tau_0 = 400$ ns, $\sigma_\tau = 2$ ns, $\mu^\phi = \pi/5$, $\kappa = 0$, $M_R = 100$, $\delta_R = \lambda/2$, $\beta_R = \pi/4$, $t = 0$ s).

A. Array-Variant TOA-AOA Joint PDF

In Fig. 3, we present the STV joint PDFs of the TOA-AOA in logarithmic scale (dB) of the wideband Ellipse channel model at the extremes and center of the receiving array, i.e., at A_1^R (left), A_{50}^R (center), and A_{100}^R (right). We imposed a minimum TOA of $\tau_0 = 400$ ns and a von Mises concentration parameter $k = 0$, i.e., uniform scattering in the AOA.

On one hand, the joint PDF of the TOA-AOA at A_{50}^R (center) shows the properties imposed by the channel model such as uniformity in the AOA domain, exponential decay in the TOA domain, and independence between TOA and AOA. On the other hand, the PDFs at the extremes of the array are remarkably affected by the transformation. The resulting meandering shape of the PDFs at A_1^R and A_{100}^R shows that the TOA varies as a function of the AOA. This is most noticeable when the receiving antenna is far from the focus of the ellipse, i.e., at A_1^R and A_{100}^R , as the sum of the distances from the opposite focus (Tx) to such antennas via scatterers of the ellipse is highly variant. In the AOA domain, the uniformity imposed ($\kappa = 0$) at the center of the array is no longer valid at its ends. Two maxima of the PDF appear around $\phi_1^R \approx -\pi/2$ and $\phi_1^R \approx \pi/4$ for A_1^R and A_{100}^R , respectively, indicating a reduction of the angular spread.

These results show that, at the extremes of a large-scale array, additional delay spread may be introduced into the channel model with unforeseen consequences. This artifact of the Ellipse channel model produced by the large dimensions of the array was not considered in previous works, e.g., [26]–[28], [30], [31]. Moreover, Fig. 3 indicates that the transformation performed breaks down the separability of the joint PDF of the TOA and AOA, as the conditional distribution of the AOA given a specific TOA depends on the delay considered.

As the STV statistical properties of the channel are noticeable only when the scatterers are relatively close to any of the arrays, we will use the parameters of the channel models presented in Table I in the following unless otherwise stated. The parameters

TABLE I
PARAMETERS OF THE PDFS OF THE THREE CHANNEL MODELS

Ellipse		UDSM				Gaussian					
ϕ^R (rad)	τ (ns)	ϕ^R (rad)	r (m)	X (m)		Y (m)					
μ^ϕ	σ_{ϕ^R}	μ_τ	σ_τ	μ_X	σ_X	μ_Y	σ_Y				
$\pi/5$	$\pi/10$	400	1	$\pi/5$	$\pi/10$	11	1	8.9	3.5	6.4	3.5

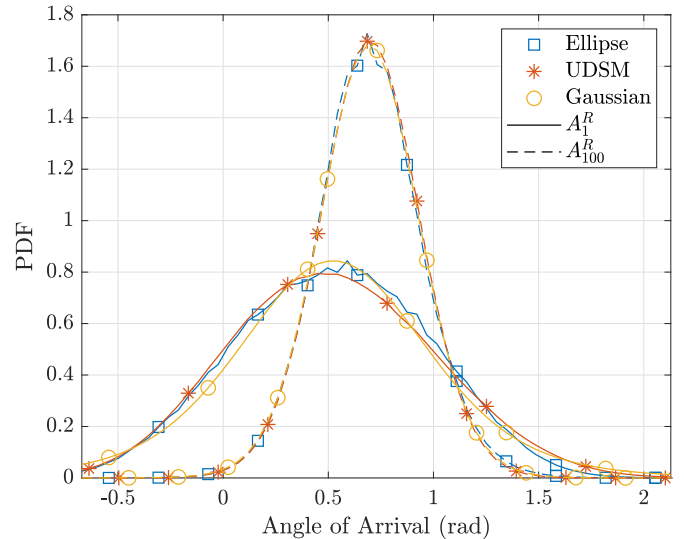


Fig. 4. Comparison of the PDFs of the AOA at the two extremes of the array for the Ellipse, modified UDSM, and Gaussian cluster channel models ($d = 100$ m, $f_c = 2$ GHz, $\tau_0 = 400$ ns, $r_0 \approx 11$ m, $\sigma_\tau = 3.4$ ns, $k_U = 10$, $\sigma_{xy} \approx 3.5$ m⁻¹, $\mu^\phi = \pi/5$, $\kappa = 10$, $M_R = 100$, $\delta_R = \lambda/2$, $\beta_R = \pi/4$, $t = 0$ s).

of the Ellipse, modified UDSM, and Gaussian cluster models are selected so that the maximum concentrations of the scatterers of all three models are coincident. The delay spread of the Ellipse model σ_τ and distance spread of the UDSM model σ_r can be chosen arbitrarily small.

B. Array-Variant Delay and Angular PSDs

In Figs. 4 and 5 we present these two marginal distributions at both extremes of the array, i.e., at A_1^R and A_{100}^R . Along with the drift of the marginal PDFs, variations of the angular and delay spreads over the array can be observed. Specifically, the mean AOA drifts approximately 0.13 rad (7 deg) and the angular spread is 0.21 rad (12 deg) higher at A_1^R than that at A_{100}^R . As it was stated above, the angular spread at A_1^R is higher because this antenna is closer to the maximum of the scattering region than A_{100}^R and it is well known that the angular size of a region is inversely proportional to the distance to it.

Moreover, as the marginal PDFs of the AOA are the same for the three models (von Mises), their variations over the array result in almost identical distributions. Note that this is consistent with the approximations used in (29) and (30) to obtain the STV parameters of the AOA distribution. Although each model presents a different marginal PDF of the TOA, a similar drift of approximately 23 ns of the mean TOA and small variations of the delay spread (below 1 ns) can be observed in Fig. 5 for the three models.

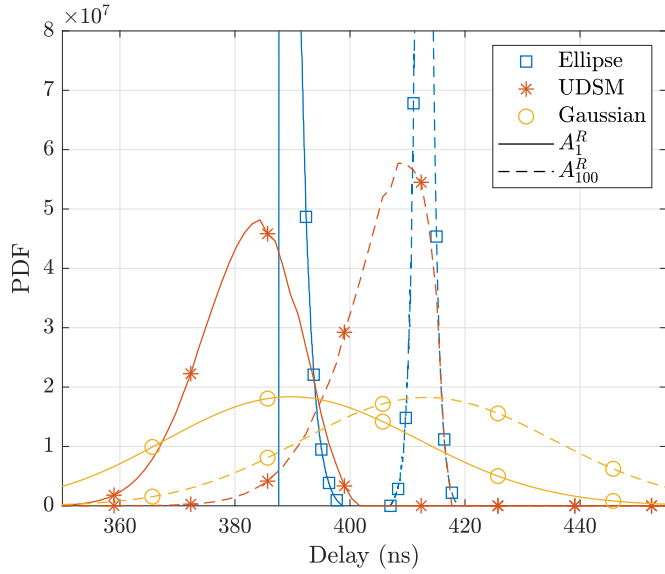


Fig. 5. Comparison of the PDFs of the TOA at the two extremes of the array for the Ellipse, modified UDSM, and Gaussian cluster channel models ($d = 100$ m, $f_c = 2$ GHz, $\tau_0 = 400$ ns, $r_0 \approx 11$ m, $\sigma_\tau = 3.4$ ns, $k_U = 10$, $\sigma_{xy} \approx 3.5$ m $^{-1}$, $\mu^\phi = \pi/5$, $\kappa = 10$, $M_R = 100$, $\delta_R = \lambda/2$, $\beta_R = \pi/4$, $t = 0$ s).

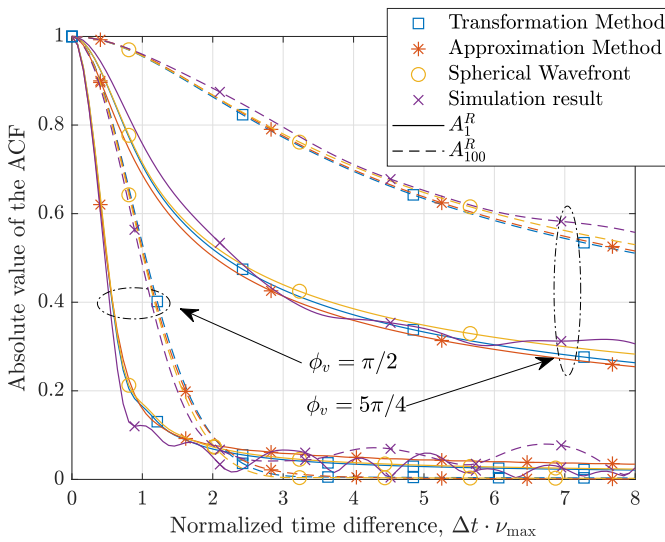


Fig. 6. Comparison of the absolute values of the local ACFs obtained by the transformation method, approximation method, spherical wavefront approach, and simulation at the two extremes of the receiving array ($d = 100$ m, $f_c = 2$ GHz, $\tau_0 = 400$ ns, $\sigma_\tau = 3.4$ ns, $\mu^\phi = \pi/5$, $\kappa = 10$, $M_R = 100$, $\delta_R = \lambda/2$, $\beta_R = \pi/4$, $\nu_{max} = 90$ Hz, $v = 13.5$ m/s, $\delta_T = 0$ m, $t = 0$).

C. Array-Variant ACF

In Fig. 6, we present a comparison of the absolute values of the array-variant local ACFs obtained by the transformation method, approximation method, spherical wavefront approach, and simulation, at the two extremes of the receiving ULA and for different directions of motion ϕ_v . Although there are small differences between the results corresponding to each method, the ACFs obtained through the transformation and approximation methods are very similar in the whole range. Moreover, the good agreement between the methods proposed and the

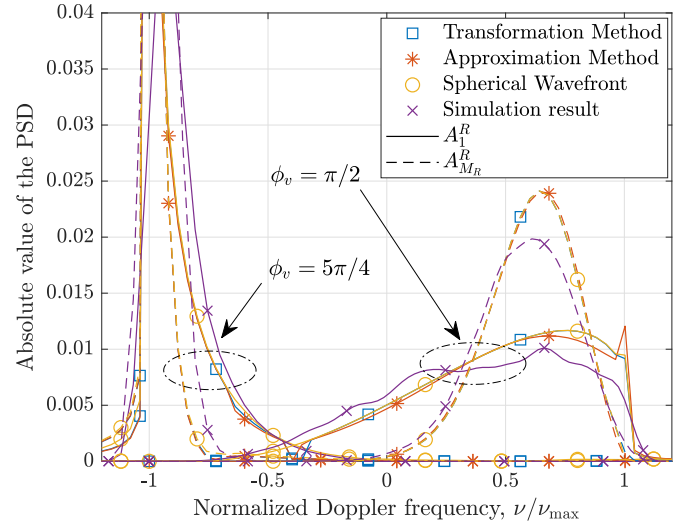


Fig. 7. Comparison of the absolute values of the local Doppler PSDs obtained by the transformation method, the approximation method, and simulation at the two extremes of the receiving array ($d = 100$ m, $f_c = 2$ GHz, $\tau_0 = 400$ ns, $\sigma_\tau = 3.4$ ns, $\mu^\phi = \pi/5$, $\kappa = 10$, $M_R = 100$, $\delta_R = \lambda/2$, $\beta_R = \pi/4$, $\nu_{max} = 90$ Hz, $v = 13.5$ m/s, $\delta_T = 0$ m, $t = 0$).

spherical wavefront approach indicates that all these methods are approximately equivalent. Note that only the ACF of the Ellipse model is presented in Fig. 6. This is because in equal conditions of motion, i.e., v and ϕ_v are equal for the three models, the ACF is only determined by the PDF of the AOA. As the PDFs of the AOA of the three models are approximately equal as shown in Fig. 4, it is not necessary to show the ACFs corresponding to the other models.

D. Array-Variant Doppler PSD

In Fig. 7, we present a comparison of the absolute values of the array-variant Doppler PSDs obtained through the transformation method, the approximation method, the spherical wavefront approach, and simulation, at the two extremes of the ULA and for different directions of motion ϕ_v . The variations of the Doppler PSD along the array can be attributed to the difference in relative motion w.r.t. the scatterers at sufficiently separated antenna elements, e.g., A_1^R and A_{100}^R . It can be seen that not only the Doppler PSD drifts along the array, but also the Doppler spread is affected. On one hand, when the ULA points to the maximum concentration of the scatterers, i.e., $\beta_R - \mu^\phi \approx 0$ or $\beta_R - \mu^\phi \approx \pi$, the Doppler PSD hardly drifts, but there is a noticeable variation of the Doppler spread along the array. On the other hand, for a perpendicular orientation of the ULA, i.e., when $\beta_R - \mu^\phi \approx \pm\pi/2$, the Doppler PSD drifts over the array, but the Doppler spread hardly varies.

E. Array-Variant S-CCF

In Fig. 8, we present a comparison of the absolute values of the array-variant receive-side S-CCFs obtained by using the transformation method, the approximation method of variant parameters, the spherical wavefront approach, and simulation,

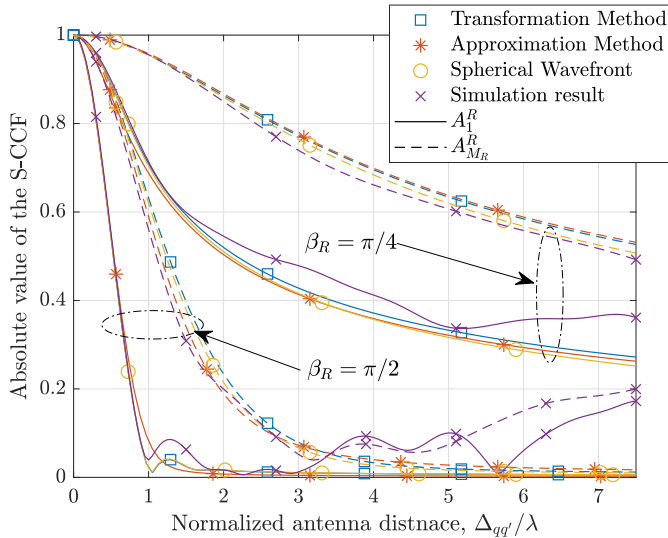


Fig. 8. Comparison of the absolute values of the local S-CCFs obtained by the transformation method, the approximation method, the spherical wavefront approach, and simulation (at the two extremes of the receiving array ($d = 100$ m, $f_c = 2$ GHz, $\tau_0 = 400$ ns, $\sigma_\tau = 3.4$ ns, $\mu^\phi = \pi/5$, $\kappa = 10$, $M_R = 100$, $\delta_R = \lambda/2$, $\beta_R = \pi/4$, $\delta_T = 0$ m, $t = 0$ s).

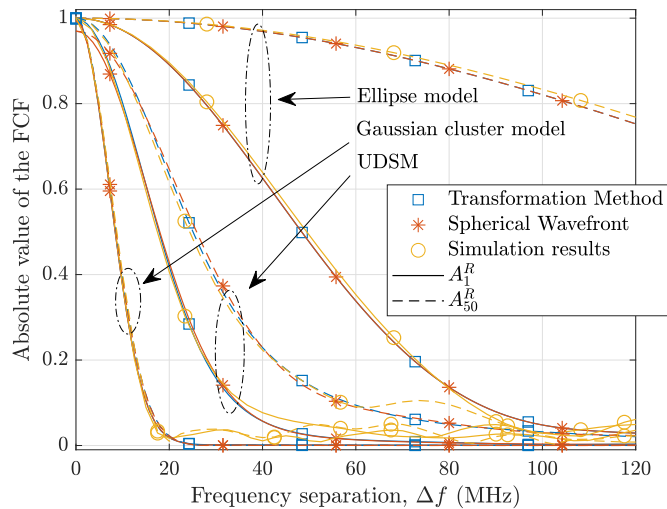


Fig. 9. Comparison of the absolute values of the local FCFs at A_1^R and A_{50}^R obtained by the transformation method, the spherical wavefront approach, and simulation ($d = 100$ m, $f_c = 2$ GHz, $\tau_0 = 400$ ns, $r_0 \approx 11$ m, $\sigma_\tau = 0.3$ ns, $k_U = 10$, $\sigma_{xy} \approx 3.5$ m $^{-1}$, $\mu^\phi = \pi/5$, $\kappa = 10$, $M_R = 100$, $\delta_R = \lambda/2$, $\beta_R = \pi/2$, $\delta_T = 0$ m, $t = 0$ s).

at the receive antenna positions A_1^R and A_{100}^R for different values of the angular tilt of the receiving antenna β_R . There is clearly a good agreement between the transformation and approximation methods proposed. The differences between the transformation and approximation methods can be attributed to the fact that the latter assumes that the function determining the PAS remains the same, e.g., von Mises (26), at any position of the array and only the parameters of that function, i.e., κ and μ^ϕ , are array-variant.

F. Array-Variant FCF

In Fig. 9, the absolute values of the array-variant FCFs of the Ellipse, modified UDSM, and Gaussian cluster models are

presented. In the figure, it can be seen that the variant distribution of the TOA results in array-variant FCFs as a consequence of the large dimensions of the receiving array. This effect is specially significant for the modified UDSM and the Ellipse model. In the last one, the imposed narrowband property ($\sigma_\tau = 0.3$ ns) or frequency flatness is slowly degraded as the distance between the center of the array and the considered antenna element increases. The cause of this artifact has already been explained in the analysis of Fig. 3. As a consequence, what it was designed as a frequency non-selective and frequency-uncorrelated channel model may change to a frequency-selective and frequency-correlated channel for sufficiently large arrays. Note that in the case of the Ellipse model we have chosen a sufficiently small value of the delay spread σ_τ to consider the channel as frequency non-selective in most practical cases, as it can be seen in the almost-flat FCF depicted for A_{50}^R . Conversely, the FCF of the Gaussian cluster model is barely affected as the shift and rotation of a 2D symmetric Gaussian distribution only affects its mean values, but not its spread. Hence, its delay PSD only experiences a shift (see Fig. 5), which affects the phase but not the absolute value of the FCF.

VII. CONCLUSION

In this article, we have proposed a novel method to model the joint PDF of the TOA and AOA in massive MIMO channels. The proposed method can be used to study massive MIMO channel characteristics of both channel measurements and models. We have also proposed an approximation method based on varying angular parameters for the von Mises distribution and obtained approximate closed-form expressions of key statistical properties of the channel. The statistical properties obtained with these two methods have shown a good agreement between them and with the spherical wavefront approach. The proposed methods incorporated the non-stationary properties of the channel model through the joint PDF of the TOA and AOA. Moreover, we showed that the means and spreads of the AOA and TOA vary over the array. Due to the delay drift and spread, we demonstrated that the FCF of massive MIMO channels is array-variant as well. Finally, it has been demonstrated that artifacts may appear when conventional MIMO models such as the Ellipse model and UDSM are applied to large-scale arrays.

APPENDIX A

TRANSFORMED PDF OF THE TOA AND AOA

For single-bounced rays, the TOA-AOA parameters of the rays (τ, ϕ^R) are related to their Cartesian coordinates in (X, Y) through the following non-linear transformation equations [40]

$$X = \frac{1}{2} \frac{(c_0\tau)^2 - d^2}{c_0\tau + d \cos \phi^R} \cos \phi^R \quad (32)$$

$$Y = \frac{1}{2} \frac{(c_0\tau)^2 - d^2}{c_0\tau + d \cos \phi^R} \sin \phi^R. \quad (33)$$

The PDF in Cartesian coordinates can be calculated by applying the theory of transformation of random variables as [40]

$$f_{X,Y}(x, y) = |J_1(x, y)|^{-1} f_{\tau, \phi^R}(\tau(x, y), \arctan(y/x)) \quad (34)$$

with $\tau(x, y) = c_0^{-1}(\sqrt{x^2 + y^2} + \sqrt{(x+d)^2 + y^2})$. $J_1(x, y)$ is the Jacobian of the transformation, i.e.,

$$|J_1(x, y)|^{-1} = c_0^{-1} \left| \frac{1}{\sqrt{x^2 + y^2}} + \frac{1 + \frac{dx}{x^2 + y^2}}{\sqrt{(x+d)^2 + y^2}} \right|. \quad (35)$$

Using $f_{X,Y}(x, y)$, we can obtain a second distribution for the antennas A_p^T and A_q^R and time instant t by performing shift and rotation operations on the random variables (X, Y) as defined by the following transformation equations

$$\begin{bmatrix} X_1 \\ Y_1 \end{bmatrix} = \begin{bmatrix} \cos \alpha_{qp}(t) & \sin \alpha_{qp}(t) \\ -\sin \alpha_{qp}(t) & \cos \alpha_{qp}(t) \end{bmatrix} \begin{bmatrix} X - x_q^R - v_x t \\ Y - y_q^R - v_y t \end{bmatrix} \quad (36)$$

where $\alpha_{qp}(t)$ denotes the angle between the segment joining A_p^T and A_q^R at time instant t and the x -axis, which can be calculated as

$$\alpha_{qp}(t) = \arctan \left(\frac{y_q^R + v_y t - y_p^T}{x_q^R + v_x t - x_p^T + d} \right). \quad (37)$$

As this transformation corresponds to a shift and rotation of the coordinate system, hence $|J_2(x_1, y_1)|^{-1} = 1$. The distribution in Cartesian coordinates is now $f_{X_1 Y_1}(x_1, y_1) = f_{XY}(x(x_1, y_1), y(x_1, y_1))$, with

$$\begin{bmatrix} x \\ y \end{bmatrix} = \begin{bmatrix} \cos \alpha_{qp}(t) & -\sin \alpha_{qp}(t) \\ \sin \alpha_{qp}(t) & \cos \alpha_{qp}(t) \end{bmatrix} \begin{bmatrix} x_1 \\ y_1 \end{bmatrix} + \begin{bmatrix} x_q^R + v_x t \\ y_q^R + v_y t \end{bmatrix}. \quad (38)$$

In the third step, the random variables (X_1, Y_1) are transformed back into the TOA-AOA domain (τ_1, ϕ_1^R) by using the inverse transformation equations of (32) and (33) used in the first step, i.e.,

$$\tau_1 = c_0^{-1} \left(\sqrt{X_1^2 + Y_1^2} + \sqrt{[X_1 + d_{qp}(t)]^2 + Y_1^2} \right) \quad (39)$$

$$\phi_1^R = \arctan(Y_1/X_1) \quad (40)$$

where the separation $d_{qp}(t)$ between A_p^T and A_q^R depends on the antennas locations at any time as

$$d_{qp}(t) = \sqrt{(x_q^R + v_x t - d - x_p^T)^2 + (y_q^R + v_y t - y_p^T)^2}. \quad (41)$$

Thus, the joint PDF of the random variables (τ_1, ϕ_1^R) can be computed as

$$\begin{aligned} f_{\tau_1, \phi_1^R}(\tau_1, \phi_1^R; \delta_q^R, \delta_p^T, t) &= |J_3(\tau_1, \phi_1^R)|^{-1} \\ &\times f_{X_1 Y_1}(x_1(\tau_1, \phi_1), y_1(\tau_1, \phi_1)) \end{aligned} \quad (42)$$

where

$$x_1(\tau_1, \phi_1) = \frac{1}{2} \frac{(c_0 \tau_1)^2 - d_{qp}^2(t)}{c_0 \tau_1 + d_{qp}(t) \cos \phi_1^R} \cos \phi_1^R \quad (43)$$

$$y_1(\tau_1, \phi_1) = \frac{1}{2} \frac{(c_0 \tau_1)^2 - d_{qp}^2(t)}{c_0 \tau_1 + d_{qp}(t) \cos \phi_1^R} \sin \phi_1^R \quad (44)$$

and $J_3(\tau_1, \phi_1^R)$ is the Jacobian of the transformation, i.e.,

$$\begin{aligned} |J_3(\tau_1, \phi_1^R)|^{-1} &= \frac{c_0}{4} \left| \frac{[(c_0 \tau_1)^2 - d_{qp}^2(t)]}{[d_{qp}(t) \cos \phi_1^R + c_0 \tau_1]^3} \right. \\ &\quad \left. \times [(c_0 \tau_1)^2 + d_{qp}^2(t) + 2d_{qp}(t)c_0 \tau_1 \cos \phi_1^R] \right|. \end{aligned} \quad (45)$$

Finally, the resulting joint PDF $f_{\tau_1, \phi_1^R}(\tau_1, \phi_1^R)$ in (9) is obtained using (34)–(45).

APPENDIX B

DERIVATION OF THE STV PARAMETERS OF THE VON MISES DISTRIBUTION

Let us use the Gaussian cluster model defined in (20) whose marginal distribution of the AOA approximates very well a von Mises distribution. The distribution of the position of the scatterers in the Gaussian cluster model expressed in polar coordinates (R, ϕ^R) can be obtained by applying the transformation equations $X = R \cos \phi^R$ and $Y = R \sin \phi^R$ as

$$f_{R, \phi^R}(r, \phi^R) = \frac{r}{2\pi \sigma_{xy}^2} e^{-\frac{1}{2\sigma_{xy}^2}(r^2 + r_c^2 - 2rr_c \cos(\phi^R - \mu_c^\phi))} \quad (46)$$

where $r_c^2 = x_0^2 + y_0^2$ and $\mu_c^\phi = \arctan(y_0/x_0)$ have been used. Clearly, the conditional distribution $f_{r, \phi^R}(\phi^R | r = r_c)$ follows a von Mises distribution with mean angle μ_c^ϕ and concentration parameter $\kappa_c = r_c^2/\sigma_c^2$. Integrating (46) w.r.t. r , the distribution of the AOA is given by

$$\begin{aligned} f_{\phi^R}(\phi^R) &= \frac{e^{-(r_c/\sqrt{2}\sigma_{xy})^2}}{2\pi} \\ &+ \frac{1}{2\sqrt{2\pi}\sigma_{xy}} \left[1 + \operatorname{erf} \left(\frac{r_c}{\sqrt{2}\sigma_{xy}} \cos(\phi^R - \mu_c^\phi) \right) \right] \\ &\times \cos(\phi^R - \mu_c^\phi) e^{-(r_c/\sqrt{2}\sigma_{xy})^2 \sin^2(\phi^R - \mu_c^\phi)}. \end{aligned} \quad (47)$$

It can be seen that (47) is a very good approximation of the von Mises distribution with mean angle μ_c^ϕ and concentration parameter $\kappa_c = (r_c/\sigma_{xy})^2$ for $\kappa \gg 1$. In practice, a root mean square error below 1% is obtained for any value of κ_c . Using the previous observation, the STV concentration parameter can be calculated as $\kappa_q^2(t) = (r_{c,q}(t)/\sigma_{xy})^2$, where $r_{c,q}(t)$ can be obtained by applying the law of cosines as

$$\begin{aligned} r_{c,q}^2(t) &= r_c^2 + (\delta_q^R)^2 + (vt)^2 - 2r_c \delta_q^R \cos(\mu_c^\phi - \beta_R) \\ &\quad - 2r_c vt \cos(\mu_c^\phi - \phi_v) + 2\delta_q^R vt \cos(\beta_R - \phi_v). \end{aligned} \quad (48)$$

Next, the distance r_c and the parameters of the von Mises distribution imposed at the center of the receiving array μ_c^ϕ and κ_c can be used to obtain the standard deviation of the Gaussian cluster model as $\sigma_{xy} = r_c/\sqrt{\kappa_c}$. The STV concentration parameter $\kappa_{qp}(t)$ in (29) can be computed substituting (48) in $\frac{r_{c,q}^2(t)}{r_c^2} \kappa$. Finally, by geometrical considerations, the

STV mean AOA $\mu_{gp}^{\phi}(t)$ can be easily obtained as indicated in (30).

REFERENCES

- [1] E. G. Larsson, O. Edfors, F. Tufvesson, and T. L. Marzetta, "Massive MIMO for next generation wireless systems," *IEEE Commun. Mag.*, vol. 52, no. 2, pp. 186–195, Feb. 2013.
- [2] C. X. Wang *et al.*, "Cellular architecture and key technologies for 5G wireless communication networks," *IEEE Commun. Mag.*, vol. 52, no. 2, pp. 122–130, Feb. 2014.
- [3] E. Björnson, E. G. Larsson, and T. L. Marzetta, "Massive MIMO: Ten myths and one critical question," *IEEE Commun. Mag.*, vol. 54, no. 2, pp. 114–123, Feb. 2016.
- [4] C. Shepard *et al.*, "Argos: Practical many-antenna base stations," in *Proc. 18th Annu. Int. Conf. Mobile Comput. Netw.*, Istanbul, Turkey, Aug. 2012, pp. 53–64.
- [5] J. Vieira *et al.*, "A flexible 100-antenna testbed for massive MIMO," in *Proc. IEEE GLOBECOM'14*, Austin, USA, Dec. 2014, pp. 287–293.
- [6] P. Harris *et al.*, "LOS throughput measurements in real-time with a 128-antenna massive MIMO testbed," in *Proc. IEEE GLOBECOM'16*, Washington, DC, USA, Dec. 2016, pp. 1–7.
- [7] D. Tse and P. Viswanath, *Fundamentals of Wireless Communication*, 1st ed., MA, USA: Cambridge Univ. Press, 2005.
- [8] X. Gao, F. Tufvesson, O. Edfors, and F. Rusek, "Measured propagation characteristics for very-large MIMO at 2.6 GHz," in *Proc. IEEE ASILOMAR'12*, Pacific Grove, USA, Nov. 2012, pp. 295–299.
- [9] X. Gao, F. Tufvesson, and O. Edfors, "Massive MIMO channels - Measurements and models," in *Proc. IEEE ASILOMAR'13*, Pacific Grove, USA, Nov. 2013, pp. 280–284.
- [10] W. Li, L. Liu, C. Tao, Y. Lu, J. Xiao, and P. Liu, "Channel measurements and angle estimation for massive MIMO systems in a stadium," in *Proc. IEEE ICACT'15*, Seoul, South Korea, Jul. 2015, pp. 105–108.
- [11] S. Payami and F. Tufvesson, "Channel measurements and analysis for very large array systems at 2.6 GHz," in *Proc. IEEE EUCAP'12*, Prague, Czech Republic, Mar. 2012, pp. 433–437.
- [12] S. Payami and F. Tufvesson, "Delay spread properties in a measured massive MIMO system at 2.6 GHz," in *Proc. IEEE PIMRC'13*, London, U.K., Sep. 2013, pp. 53–57.
- [13] X. Gao, O. Edfors, F. Rusek, and F. Tufvesson, "Massive MIMO performance evaluation based on measured propagation data," *IEEE Trans. Wireless Commun.*, vol. 14, no. 7, pp. 3899–3911, Jul. 2015.
- [14] X. Gao, O. Edfors, F. Tufvesson, and E. G. Larsson, "Massive MIMO in real propagation environments: Do all antennas contribute equally?," *IEEE Trans. Commun.*, vol. 63, no. 11, pp. 3917–3928, Nov. 2015.
- [15] C.-X. Wang, S. Wu, L. Bai, X. You, J. Wang, and I. Chih-Lin, "Recent advances and future challenges for massive MIMO channel measurements and models," *Sci. China Inf. Sci.*, vol. 59, no. 2, pp. 1–16, Feb. 2016.
- [16] J. Huang, C. X. Wang, R. Feng, J. Sun, W. Zhang, and Y. Yang, "Multi-frequency mmWave massive MIMO channel measurements and characterization for 5G wireless communication systems," *IEEE J. Sel. Areas Commun.*, vol. 35, no. 7, pp. 1591–1605, Jul. 2017.
- [17] C.-X. Wang, J. Bian, J. Sun, W. Zhang, and M. Zhang, "A survey of 5G channel measurements and models," *IEEE Commun. Surv. Tut.*, vol. 20, no. 4, pp. 3142–3168, Oct.–Dec. 2018.
- [18] G. Matz, "On non-WSSUS wireless fading channels," *IEEE Trans. Wireless Commun.*, vol. 4, no. 5, pp. 2465–2478, Sep. 2005.
- [19] A. Gehring, M. Steinbauer, I. Gaspard, and M. Grigat, "Empirical channel stationarity in urban environments," in *Proc. EPMCC'01*, Vienna, Austria, Feb. 2001.
- [20] C. X. Wang, A. Ghazal, B. Ai, Y. Liu, and P. Fan, "Channel measurements and models for high-speed train communication systems: A survey," *IEEE Commun. Surv. Tut.*, vol. 18, no. 2, pp. 974–987, Apr.–Jun. 2016.
- [21] J. Yang *et al.*, "A geometry-based stochastic channel model for the millimeter-wave band in a 3GPP high-speed train scenario," *IEEE Trans. Veh. Technol.*, vol. 67, no. 5, pp. 3853–3865, May 2018.
- [22] T. Zwick, C. Fischer, D. Didascalou, and W. Wiesbeck, "A stochastic spatial channel model based on wave-propagation modeling," *IEEE J. Sel. Areas Commun.*, vol. 18, no. 1, pp. 6–15, Jan. 2000.
- [23] C.-C. Chong, D. I. Laurenson, and S. McLaughlin, "The implementation and evaluation of a novel wideband dynamic directional indoor channel model based on a Markov process," in *Proc. IEEE PIMRC'03*, Beijing, China, Sep. 2003, pp. 670–674.
- [24] L. Correia, *Mobile Broadband Multimedia Networks*, 1st ed. Oxford, U.K.: Academic Press, 2006.
- [25] R. Verdone and A. Zannella, *Pervasive Mobile and Ambient Wireless Communications – The COST Action 2100*, 1st ed. Berlin, Germany: Springer, 2011.
- [26] S. Wu, C.-X. Wang, H. Haas, H. Aggoune, M. M. Alwakeel, and B. Ai, "A non-stationary wideband channel model for massive MIMO communication systems," *IEEE Trans. Wireless Commun.*, vol. 14, no. 3, pp. 1434–1446, Mar. 2015.
- [27] S. Wu, C. X. Wang, E. H. M. Aggoune, M. M. Alwakeel, and Y. He, "A non-stationary 3-D wideband twin-cluster model for 5G massive MIMO channels," *IEEE J. Sel. Areas Commun.*, vol. 32, no. 6, pp. 1207–1218, Jun. 2014.
- [28] S. Wu, C. X. Wang, el-H. M. Aggoune, M. M. Alwakeel, and X. H. You, "A general 3D non-stationary 5G wireless channel model," *IEEE Trans. Commun.*, vol. 66, no. 7, pp. 3065–3078, Jul. 2018.
- [29] Y. Liu, C. Wang, J. Huang, J. Sun, and W. Zhang, "Novel 3-D non-stationary mmwave massive MIMO channel models for 5G high-speed train wireless communications," *IEEE Trans. Veh. Technol.*, vol. 68, no. 3, pp. 2077–2086, Mar. 2019.
- [30] C. F. López, C.-X. Wang, and R. Feng, "A novel 2D non-stationary wideband massive MIMO channel model," in *Proc. IEEE CAMAD'16*, Toronto, Canada, Oct. 2016, pp. 207–212.
- [31] C. F. López and C.-X. Wang, "Novel 3D non-stationary wideband models for massive MIMO channels," *IEEE Trans. Wireless Commun.*, vol. 17, no. 5, pp. 2893–2905, May 2018.
- [32] J. Jung, E. Kurniawan, and S. Sun, "Channel correlation modeling and its application to massive MIMO channel feedback reduction," *IEEE Trans. Veh. Technol.*, vol. 66, no. 5, pp. 3787–3797, May 2017.
- [33] S. Jaeckel, L. Raschkowski, K. Börner, and L. Thiele, "QuADriGa: A 3-D multi-cell channel model with time evolution for enabling virtual field trials," *IEEE Trans. Antennas Propag.*, vol. 62, no. 6, pp. 3242–3256, Jun. 2014.
- [34] M. Peter *et al.*, "Measurement campaigns and initial channel models for preferred suitable frequency ranges," mmMagic Project, Tech. Rep. D2.1 V1.0, 2016.
- [35] L. Raschkowski *et al.*, "METIS channel models (D1.4)," ICT-317669 METIS Project, Tech. Rep. ICT-317669, Jul. 2015.
- [36] G. T. 38.901, "Study on channel model for frequencies from 0.5 to 100 GHz," Tech. Rep. V14.3.0, 2017.
- [37] I.-R. R15-WP5D-170613-TD-0332, "Preliminary draft new report ITU-R M.[IMT-2020.EVAL], test environments and channel models," 3GPP, Tech. Rep. TR 38.901, V14.3.0, Jun. 2017.
- [38] X. Gao, J. Flordelis, G. Dahman, F. Tufvesson, and O. Edfors, "Massive MIMO channel modeling - Extension of the COST 2100 model," in *Proc. JNCW'15*, Barcelona, Spain, Oct. 2015, pp. 1–8.
- [39] A. Malteva *et al.*, "Channel modeling and characterization," ICT FP7 MiWEBA Project, Tech. Rep. D5.1 V1.0, Jun. 2014.
- [40] A. Borhani and M. Pätzold, "On the spatial configuration of scatterers for given delay-angle distributions," *IAENG Eng. Lett.*, vol. 22, no. 1, pp. 34–38, Feb. 2014.
- [41] R. B. Ertel and J. H. Reed, "Angle and time of arrival statistics for circular and elliptical scattering models," *IEEE J. Sel. Areas Commun.*, vol. 17, no. 11, pp. 1829–1840, Nov. 1999.
- [42] S. H. Kong, "TOA and AOD statistics for down link Gaussian scatterer distribution model," *IEEE Trans. Wireless Commun.*, vol. 8, no. 5, pp. 2609–2617, May 2009.
- [43] C.-F. Lopez and C.-X. Wang, "A study of delay drifts on massive MIMO wideband channel models," in *Proc. IEEE WSA'18*, Bochum, Germany, Mar. 2018, pp. 1–7.
- [44] M. Pätzold, *Mobile Radio Channels*, 2nd ed., West Sussex: NJ, USA: Wiley, 2012.
- [45] A. Ghazal, C. X. Wang, B. Ai, D. Yuan, and H. Haas, "A nonstationary wideband MIMO channel model for high-mobility intelligent transportation systems," *IEEE Trans. Intell. Transp. Syst.*, vol. 16, no. 2, pp. 885–897, Apr. 2015.
- [46] Y. Liu, C.-X. Wang, C.-F. Lopez, and X. Ge, "3D non-stationary wideband circular tunnel channel models for high-speed train wireless communication systems," *Sci. China Inf. Sci.*, vol. 60, no. 8, Aug. 2017.
- [47] A. Ghazal *et al.*, "A non-stationary IMT-Advanced MIMO channel model for high-mobility wireless communication systems," *IEEE Trans. Wireless Commun.*, vol. 16, no. 4, pp. 2057–2068, Apr. 2017.
- [48] K. Mardia and P. E. Jupp, *Directional Statistics*. NJ, USA: Wiley, 2000.

- [49] A. Y. Olenko, K. T. Wong, and E. H.-O. Ng, "Analytically derived TOA-DOA statistics of uplink/downlink wireless multipaths arisen from scatterers on a hollow-disc around the mobile," *IEEE Antennas Wireless Propag. Lett.*, vol. 2, no. 1, pp. 345–348, 2003.
- [50] A. Borhani and M. Pätzold, "A unified disk scattering model and its angle-of-departure and time-of-arrival statistics," *IEEE Trans. Veh. Technol.*, vol. 62, no. 2, pp. 473–485, Feb. 2013.
- [51] Y. Yuan, C. X. Wang, Y. He, M. M. Alwakeel, and el-H. M. Aggoune, "3D wideband non-stationary geometry-based stochastic models for non-isotropic MIMO vehicle-to-vehicle channels," *IEEE Trans. Wireless Commun.*, vol. 14, no. 12, pp. 6883–6895, Dec. 2015.
- [52] L. Devroye, *Non-Uniform Random Variate Generation*, 1st ed., New York, USA: Springer-Verlag, 1986.



Carlos F. López received the B.Sc. and M.Sc. degrees in telecommunications engineering from the Technical University of Madrid, Spain, in 2011 and 2015, respectively, and the Ph.D. degree in wireless communications from Heriot-Watt University, U.K., in 2019.

In 2011, he was a Research Engineer with the Radio Communication Research Group, Technical University of Madrid, where he led the design and development of simulation tools for wireless channel modeling in 4G/LTE mobile communications networks and he carried out measurement campaigns for wireless channel characterization using broadband communication systems in Madrid Metro facilities. From 2015 to 2018, he was a Research Associate and a Ph.D. candidate with Heriot-Watt University, Edinburgh, U.K. Since 2018, he has been a Software Engineer with the Wireless Standards Team, The MathWorks. His research interests include wireless channel measurements, modeling, and simulation, massive MIMO systems, and mm-Wave wireless communications.



Cheng-Xiang Wang (Fellow, IEEE) received the B.Sc. and M.Eng. degrees in communication and information systems from Shandong University, China, in 1997 and 2000, respectively, and the Ph.D. degree in wireless communications from Aalborg University, Denmark, in 2004.

He was a Research Assistant with the Hamburg University of Technology, Hamburg, Germany, from 2000 to 2001, a Visiting Researcher with Siemens AG Mobile Phones, Munich, Germany, in 2004, and a Research Fellow with the University of Agder, Grimstad, Norway, from 2001 to 2005. He has been with Heriot-Watt University, Edinburgh, U.K., since 2005, where he was promoted to a Professor in 2011. Since 2018, he has been with Southeast University, China, as a Professor. He is also a part-time Professor with Purple Mountain Laboratories, Nanjing, China. He has authored four books, two book chapters, and more than 400 papers in refereed journals and conference proceedings, including 24 Highly Cited Papers. He has also delivered 22 Invited Keynote Speeches/Talks and 7 Tutorials in international conferences. His current research interests include wireless channel measurements and modeling, B5G wireless communication networks, and applying artificial intelligence to wireless communication networks.

Prof. Wang is a member of the Academia Europaea, a fellow of the IET, an IEEE Communications Society Distinguished Lecturer in 2019 and 2020, and a Highly-Cited Researcher recognized by Clarivate Analytics, in 2017–2020. He is currently an Executive Editorial Committee Member for the IEEE TRANSACTIONS ON WIRELESS COMMUNICATIONS. He was an Editor for nine international journals, including the IEEE TRANSACTIONS ON WIRELESS COMMUNICATIONS from 2007 to 2009, the IEEE TRANSACTIONS ON VEHICULAR TECHNOLOGY from 2011 to 2017, and the IEEE TRANSACTIONS ON COMMUNICATIONS from 2015 to 2017. He was a Guest Editor for the IEEE JOURNAL ON SELECTED AREAS IN COMMUNICATIONS, *Special Issue on Vehicular Communications and Networks* (Lead Guest Editor), *Special Issue on Spectrum and Energy Efficient Design of Wireless Communication Networks*, and *Special Issue on Airborne Communication Networks*. He was also a Guest Editor for the IEEE TRANSACTIONS ON BIG DATA, *Special Issue on Wireless Big Data*, and is a Guest Editor for the IEEE TRANSACTIONS ON COGNITIVE COMMUNICATIONS AND NETWORKING, *Special Issue on Intelligent Resource Management for 5G and Beyond*. He was a TPC Member, TPC Chair, and General Chair for over 80 international conferences. He was the recipient of the twelve Best Paper Awards from IEEE GLOBECOM 2010, IEEE ICCT 2011, ITST 2012, IEEE VTC 2013-Spring, IWCMC 2015, IWCMC 2016, IEEE/CIC ICC 2016, WPMC 2016, WOCC 2019, IWCMC 2020, and WCSP 2020.